Optical coherence tomography speckle reduction by a partially spatially coherent source

Jeehyun Kim
University of Texas at Austin
College of Engineering
Department of Biomedical Engineering
Austin, Texas 78703
    and
University of California
Beckman Laser Institute
Irvine, California 92612
E-mail: jeehyun@laser.bli.uci.edu

Donald T. Miller
Indiana University
School of Optometry
Bloomington, Indiana 47405

Eunha Kim
Sanghoon Oh
Junghwan Oh
Thomas E. Milner
University of Texas at Austin
College of Engineering
Department of Biomedical Engineering
Austin, Texas 78703

Abstract. Speckle in optical coherence tomography (OCT) images originates in the high spatial coherence of incident light that enables interference of light backscattered from spatially heterogenous tissue specimens. We report results of a numerical simulation and an experiment to test speckle reduction using a partially spatially coherent source. A Gaussian-Schell model for a partially spatially coherent source is used in the OCT simulation. For the experiment, such a source was generated by a spatially coherent boardband light source and a multimode fiber. The advantage of using a multimode fiber in combination with a broadband source is the large number of photons per coherence volume. To illustrate speckle reduction with a partially spatially coherent source, we record low-coherence interferograms of a scattering surface using single-mode and multimode source fibers. Interferograms recorded using a single-mode source fiber are indicative of those observed using conventional OCT. Speckle in OCT images recorded using a multimode source fiber is substantially reduced. © 2005 Society of Photo-Optical Instrumentation Engineers.
 [DOI: 10.1117/1.2138031]

1 Introduction

Optical coherence tomography (OCT) uses the short temporal coherence properties of broadband light to extract structural information from heterogeneous samples such as tissue. Two approaches are recognized to generate 2-D and 3-D OCT images: single-point raster scanning[1–4] and parallel/wide-field imaging.[5–8] Speckle noise is a major obstacle in measuring specific structural properties (e.g., birefringence[9–11]) of tissue specimens and observing specific features that approach the diffraction limit.[12] Although speckle in OCT images is still being investigated, a common view is that the effect originates in distorted wavefronts of light returning from tissue that result in random appearing constructive and destructive features in the interferogram.

Figure 1 shows OCT images of *in vivo* primate retina and porcine mesenteric artery that present high-contrast speckle in regions of strong backscatter in two different biological tissue samples. The appearance of speckle in the retinal nerve fiber layer (RNFL) of Fig. 1(a) does not vary with depth, but rather present relatively constant over the depth. The media and adventitia area of Fig. 1(b) also display a gradual distribution of the speckle feature, indicating that the speckle is not dependent on depth because multiple backscattering and random phase variation of the returning light dominate the statistical properties of the speckle.

Speckle reduction methods have been addressed by several investigators and include postsignal processing,[13–18] angular compounding,[19–22] and use of spatially incoherent illumination.[23] Postsignal processing techniques have been reported, including a zero-amplitude procedure,[18] deconvolution, and rotating kernel transformation. The zero-amplitude procedure (ZAP), which operates in the complex number domain, shows speckle reduction in OCT images but blurs boundaries between tissue structures. Other complex-number-domain processing methods applied to OCT include iterative point deconvolution (i.e., CLEAN in Ref. 16), and constrained iterative deconvolution.[17] Deconvolution techniques require some prior knowledge of the point spread function of the imaging optics,[24] as well as the optical properties of the imaged sample. The computation time of the rotating kernel transformation (RKT) technique, applied by Rogowsk and Brezinski[14] increases substantially with kernel size. Angular compounding methods are based on acquiring/averaging multiple beams each with a different incidence/reflecting angle from the sample but have the disadvantages of either time-restricted implementation or high complexity.

Use of spatially incoherent illumination with a thermal light source has neither time constraints nor high complexity, but suffers from reduced SNR due to the low photon number

---

Address all correspondence to Jeehyun Kim, Beckman Laser Institute, 1002 Health Science Road East, UC Irvine, Irvince, CA 92612. Tel: 949–824–3754. Fax: 949–824–6969. E-mail: jeehk@uci.edu
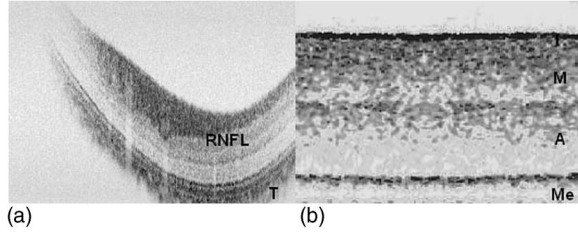
Fig. 1 Examples of OCT images with presence of speckle: (a) PS-OCT intensity image of a primate retina, inferior to the optic nerve head, where N is nasal while T is temporal and RNFL is the retinal nerve fiber layer. (b) OCT intensity image of a mesenteric artery.

per spatial mode.[23] Since the average number of photons within a coherence volume for thermal light sources is of the order of unity, these sources are nondegenerate.[25] Use of quasihomogeneous (partially spatially coherent) illumination has long been recognized to improve lateral resolution by decreasing speckle in recorded images.[25–27] Although partially spatially coherent illumination can be easily implemented using a multimode optical fiber,[28] its application in OCT imaging has not been reported, possibly due to problems associated with modal dispersion and alignment constraints.

We present a mathematical analysis and an experimental result showing a simple and rapid method to reduce speckle in OCT imaging using a partially spatially coherent light source generated by a multimode fiber. Although the coherence length of this source is reduced, the photon number per spatial mode is much larger than unity. The paper is organized as follows. First, we derive an interferometric imaging equation for an OCT system utilizing a Gaussian-Schell model light source. A numerical simulation and experimental setup are described in Sec. 2. Experimental results are presented in Sec. 3 and discussion in Sec. 4. Summary and conclusions follow in Sec. 5.

2 Theory and Methods

Figure 2 shows a two-beam imaging Michelson interferometer. Broadband and partially spatially coherent light is emitted from a source and illuminates the sample and a reference mirror, which are imaged onto a CCD camera by lens L3. Spatial coordinates at the sample, reference, and CCD camera are denoted by (ξ,ζ), (ξ',ζ'), and (x,z) respectively, where ξ, ξ', and x are in a plane perpendicular to light propagation, while ζ, ζ', and z are along a line parallel to light propagation. The amplitude of light A_s at the CCD camera plane produced from the sample reflection can be written as a coherent integral[29] of amplitudes reflected from the sample modulated by point-spread function $[h(\cdot)]$ and the local reflectivity $[r(\xi)]$,

$$A_s(x,\nu) = \int_{-\infty}^{\infty} A_i(\xi,\nu)r(\xi)\exp(-2\pi j\nu\tau)h(x-\xi,\nu)\mathrm{d}\xi, \quad (1)$$

where subscripts s indicates sample. The factor $\exp(-j2\pi\nu\tau)$ is included to account for the optical path length difference between reference and sample paths and will become important when sample and reference beams are combined. In Eq. (1) we assume amplitude of light returning from
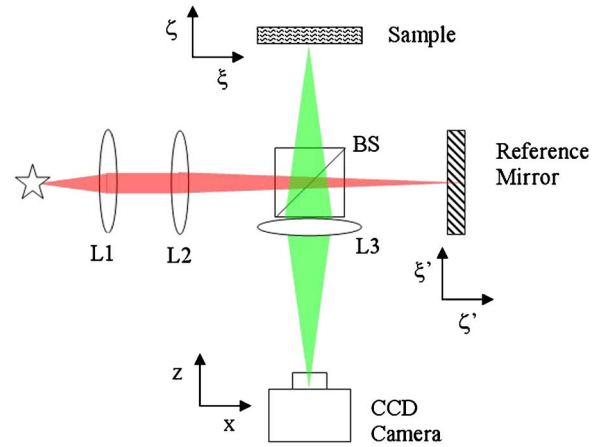

Fig. 2 Imaging Michelson interferometer with wide-field illumination.

the sample is the simple product of the incident amplitude $[A_i(\xi,\nu)]$ and local reflectivity $[r(\xi)]$. In thick heterogeneous media such as tissue, the amplitude of light returning from the sample is an integral of incident amplitude and tissue refractive index $[n(\xi)]$. Similarly the amplitude field A_r at the CCD camera plane imaged from the reference mirror can be written as

$$A_r(x,\nu) = \int_{-\infty}^{\infty} A_i(\xi',\nu)r_{\mathrm{mir}}h(x-\xi',\nu)\mathrm{d}\xi', \quad (2)$$

where subscripts r indicates the reference, and r_{mir} is a constant reflectivity of the mirror. When sample and reference fields (A_s and A_r) interfere at the image plane, intensity at position x consists of two dc intensity components and a fringe signal. The fringe signal is a complex correlation between amplitudes returned from sample and reference paths. The detected signal can be written as

$$I_d(x,\nu,\tau) = \langle|A_s(x,\nu,\tau)+A_r(x,\nu)|^2\rangle = I_s(x,\nu)+I_r(x,\nu)$$
$$+ 2\,\mathrm{Re}\langle A_s(x,\nu,\tau)A_r^*(x,\nu)\rangle, \quad (3)$$

where $I_s(x,\nu)$ and $I_r(x,\nu)$ are the dc intensities from sample and reference paths, respectively, represented by

$$I_s(x,\nu) = \int\int \langle A_i^*(\xi'',\nu,\tau)A_i(\xi,\nu,\tau)\rangle$$
$$\times r^*(\xi'')r(\xi)h^*(x-\xi'',\nu)h(x-\xi,\nu)\mathrm{d}\xi\,\mathrm{d}\xi'', \quad (4a)$$

$$I_r(x,\nu) = \int\int \langle A_i(\xi',\nu)A_i^*(\xi''',\nu)\rangle$$
$$\times|r_{\mathrm{mir}}|^2 h(x-\xi',\nu)h^*(x-\xi''',\nu)\mathrm{d}\xi'\,\mathrm{d}\xi'''. \quad (4b)$$

Expressions for $I_s(x,\nu)$ and $I_r(x,\nu)$ are the well-known imaging equations for partially spatial coherent light.[25]

The complex fringe signal optical frequency (ν) is given by,

$$I_f(x, \nu, \tau) = \langle A_s(x, \nu, \tau) A_r^*(x, \nu) \rangle$$

$$= r_{mir} \int_{-\infty}^{\infty} \int_{-\infty}^{\infty} \langle A_i(\xi, \nu) A_i^*(\xi', \nu) \rangle r^*(\xi)$$

$$\times \exp(-j2\pi\nu\tau) h(x - \xi, \nu) h^*(x - \xi', \nu) d\xi \, d\xi'. \tag{5}$$

Inclusion of the complex sample reflectivity $[r(\xi)]$ distinguishes the interference imaging equation [Eq. (5)] from reference and sample intensity integrals [Eq. (4)].

By summing over optical frequencies (ν) the expression for the complex fringe signal $I_f(x, \tau)$ becomes

$$I_f(x, \tau) = \int_{-\infty}^{\infty} \langle A_s(x, \nu, \tau) A_r^*(x, \nu) \rangle d\nu. \tag{6}$$

We model Eq. (6) with a Gaussian-Schell model source. The Gaussian-Schell model expression of the complex fringe can be written as

$$I_f(x, \tau) = r_{mir} \int_{-\infty}^{\infty} \int_{-\infty}^{\infty} \int_{-\infty}^{\infty} W(\xi, \xi', \nu) r(\xi)$$

$$\times \exp(-j2\pi\nu\tau) h(x - \xi) h^*(x - \xi') d\xi \, d\xi' \, d\nu, \tag{7}$$

where we have neglected the optical frequency (ν) dependence of the point-spread function $[h( )]$ and local reflectivity $[r(\xi)]$. Here $W(\xi, \xi', \nu)$ is the cross-spectral density function, and has the coherent-mode representation[30]

$$W(\xi_1, \xi_2, \omega) = \sum_n \alpha_n(\omega) \varphi_n^*(\xi_1, \omega) \varphi_n(\xi_2, \omega), \tag{8}$$

where the asterisk denotes the complex conjugate. The functions $\varphi_n(\xi, \omega)$ are the eigenfunctions (modes), and the coefficients $\alpha_n(\omega)$ are the eigenvalues of the integral equation. From the physical viewpoint, Eq. (8) indicates that a partially coherent source can be represented as a superposition of mutually uncorrelated modes each of which is spatially completely coherent in the space-frequency domain.[31] For the simulation study we model the cross-spectral density function $[W(\xi, \xi', \nu)]$ as a Gaussian-Schell model source, having the form

$$W(\xi, \xi', \nu) = [S(\xi, \nu)]^{1/2} [S(\xi', \nu)]^{1/2} g(\xi - \xi', \nu), \tag{9}$$

with

$$S(\xi, \nu) = A^2(\nu) \exp[-\xi^2/2\sigma_s^2(\nu)], \tag{10}$$

$$g(\xi - \xi', \nu) = \exp[-(\xi - \xi')^2/2\sigma_g^2(\nu)], \tag{11}$$

representing the spectral density and the spectral degree of coherence of light with positive values σ_s and σ_g. The source power spectral density is given by $A^2(\nu)$. Values of σ_s and σ_g, which generally depend on optical frequency (ν), determine the effective widths of the beam and spatial coherence, across the beam spot at the detection plane imaged from the sample and the reference mirror, respectively. The limit $\sigma_g \ll \sigma_s$ represents a globally incoherent (the so-called quasihomogeneous) source, while the opposite limit $\sigma_g \gg \sigma_s$ corresponds to a completely coherent source. The point spread function with a square aperture with width D is

$$h(x - \xi) = \mathrm{sinc}\left[\frac{D}{cz} \nu_0 (x - \xi)\right], \tag{12}$$

where z is the distance between the sample and lens, c is speed of light, and ν_0 is center optical frequency of the source power spectral density.

If the power spectral density $A^2(\nu)$ is given as

$$A^2(\nu) = \exp\left[-\frac{(\nu - \nu_0)^2}{2\Delta\nu^2}\right], \tag{13}$$

where $\Delta\nu$ is the FWHM spectral width of the source, we can evaluate Eq. (7). Substituting Eqs. (9)–(12) into the complex fringe signal [Eq. (7)] and integrating over ν, we find

$$I_f(x, \tau) = \sqrt{\pi} \exp(-i\pi\tau\nu_0) \exp\left(-\frac{\pi^2\tau^2}{2\Delta\nu^2}\right)$$

$$\times \int \int \mathrm{sinc}\left[\frac{D}{cz} \nu_0 (x - \xi)\right] \mathrm{sinc}\left[\frac{D}{cz} \nu_0 (x - \xi')\right] r(\xi)$$

$$\times \left[\frac{1}{2\Delta\nu^2} + A(\xi, \xi')\right] \exp[-A(\xi, \xi')\pi^2\tau^2] d\xi \, d\xi', \tag{14}$$

where σ_s and σ_g are dependent on optical frequency (ν) and estimated as $\sigma_s(\nu_0)(\nu_0/\nu)$ and $\sigma_g(\nu_0)(\nu_0/\nu)$, respectively, and $A(\xi, \xi')$ is

$$A(\xi, \xi') = \frac{\sigma_g(\nu_0)^2(\xi^2 + \xi'^2) + 2\sigma_s(\nu_0)^2(\xi - \xi')^2}{4\sigma_s(\nu_0)^2\sigma_g(\nu_0)^2\nu_0^2}.$$

We note that the complex fringe signal $I_f(x, \tau)$ in Eq. (14) contains the OCT complex fringe signal with carrier frequency $[\exp(-i\pi\tau\nu_0)]$ with envelope $[\exp(-\pi^2\tau^2/2\Delta\nu^2)]$, but also a multiplicative term, which is the integral over spatial coordinates $[\xi, \xi']$. The integral over ξ and ζ' accumulates in regions where the point spread functions are nonzero and is proportional to $r(\xi)$. Because the phase of $r(\xi)$ can fluctuate with sample position (ξ), the multiplicative term introduces speckle.

Because the exact form of the complex reflectivity of the sample $[r(\xi)]$ is not generally known, we evaluate the statistics of $I_f(x, \tau)$. We assume that the local complex reflectivity $[r(\xi)]$ in a sample has a fixed amplitude distribution $[r(\xi)]$ with randomly varying but uniformly distributed phase[19] (ϕ_k). The complex fringe signal at position x in Eq. (14) can be viewed as a sum of all field amplitudes reflected back within a coherence patch. Each field amplitude reflected from the sample contributes as a complex-valued phasor at position x in the observation plane. The complex fringe signal with speckle can be analyzed as a random phasor sum:

$$I_f = a \exp(i\theta) = \frac{1}{N} \sum_{k=1}^{N} \alpha_k \exp(i\phi_k). \tag{15}$$

The amplitude (α_k) represents the comprehensive amplitude terms in Eq. (14) and $\exp(i\phi_k)$ is the randomly varying phase
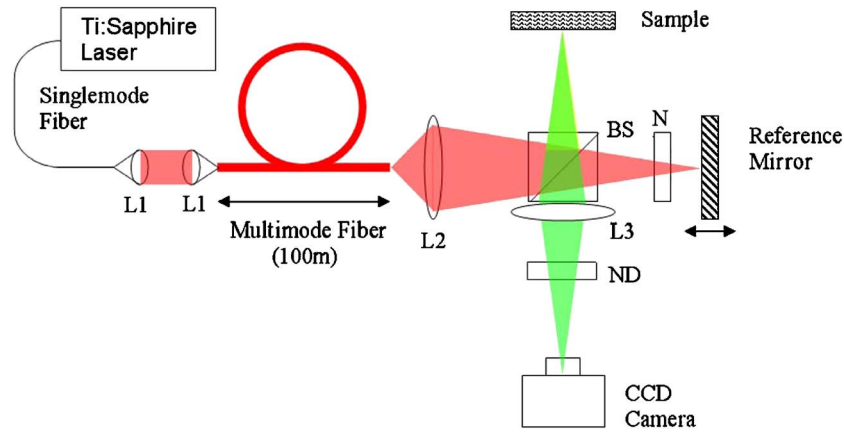
Fig. 3 Optical setup with multimode fiber in source path of Michelson interferometer: L1 ($f=10$ mm), L2 ($f=150$ mm), and L3 ($f=100$ mm); lenses; BS; beamsplitter; ND, neutral density filter.

of the complex reflectivity of the sample. The probability density function of the amplitude of the random phasor sum follows a Rayleigh function and has mean and variance:

$$\bar{a} = \sqrt{\frac{\pi}{2}}\sigma,$$

$$\sigma_a^2 = \left(2 - \frac{\pi}{2}\right)\sigma^2, \qquad (16)$$

where σ^2 is the second moment $\overline{\alpha^2}$ divided by two. The mean and variance of the amplitude are dependent only on and proportional to the second moment $\overline{\alpha^2}$. Although the second moment of the complex fringe signal can be calculated analytically by finding the second derivative of a characteristic function after integrating over ξ' in Eq. (14), this study includes a numerical evaluation of the second moment of the complex fringe signal [Eq. (14)] with variable coherent size (σ_g).

2.1 Numerical Simulation

Because speckle in OCT arises from coherent interference of backscattered light from the sample, we investigate speckle reduction by considering a Gaussian-Schell model source with different spatial coherence lengths (σ_g) used in conjunction with a 1-D rough surface. The complex fringe signal [Eq. (14)] is computed along a line using software written by the author. We assume pupil of lens L3 has a diameter of 1 cm and is placed 10 cm away from the sample or reference mirror giving a numerical aperture (NA)=0.1. The width of the point spread function (PSF) is calculated to be $1.2\lambda_0/NA$

$=8.5$ μm assuming $\lambda_0=850$ nm. Grid spacing for ξ and ξ' is 0.34 μm or 25 times smaller than the PSF width. Beam spot diameter (σ_s) at the sample and the reference mirror is set at $\sigma_s=100$ μm and several spatial coherent lengths (σ_g) of the Gaussian-Schell model source are chosen to observe the speckle reduction effect. The sample reflectivity is set at unity between 40 and 60 μm and zero elsewhere. Phases vary from $-\pi$ to π with uniformly distributed random probability. The image plane is positioned at 10 cm from lens L3 and complex fringe signal [$I_f(x)$] space is computed over [$x=0, 100$ μm] at discrete points separated by 1 μm.

2.2 Experimental Setup

A depth-resolving OCT system based on a two-beam Michelson interferometer was constructed to investigate speckle reduction using a partially spatial coherent source. Partially spatial coherent light was generated from a coherent light source by using a long segment of high-NA multimode optical fiber. For coherent illumination, we used a single mode fiber with a cuffoff wavelength $\lambda_c=800$ nm. Both single- and multi-mode optical fibers are placed in the source path of a Michelson interferometer to investigate effect of source coherence length on speckle reduction. First, we used a 100-m-long, 0.48-NA multimode glass optical fiber with a 200-μm core diameter, producing about 63,000 coherent spatial modes.[32] Second, we used a 30-m-long single mode optical fiber (Rifocs Corp.) similar to that used in a conventional OCT setup. In both cases, a mode-locked Ti:sapphire laser with an output centered at 850 nm and spectral width $\Delta\lambda \sim 50$ nm is coupled into the fibers and used as source light. When coupled into a single mode fiber, light gives a TEM_{00} spatial mode. In the
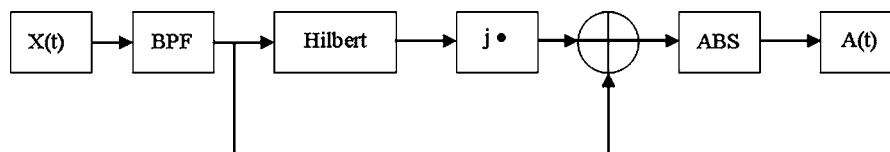

Fig. 4 Flow diagram for incoherent demodulation: $X(t)$; detected signal; BPF, bandpass filter; Hilbert, Hilbert transform; ABS, absolute value; $A(t)$, envelope of the detected signal.
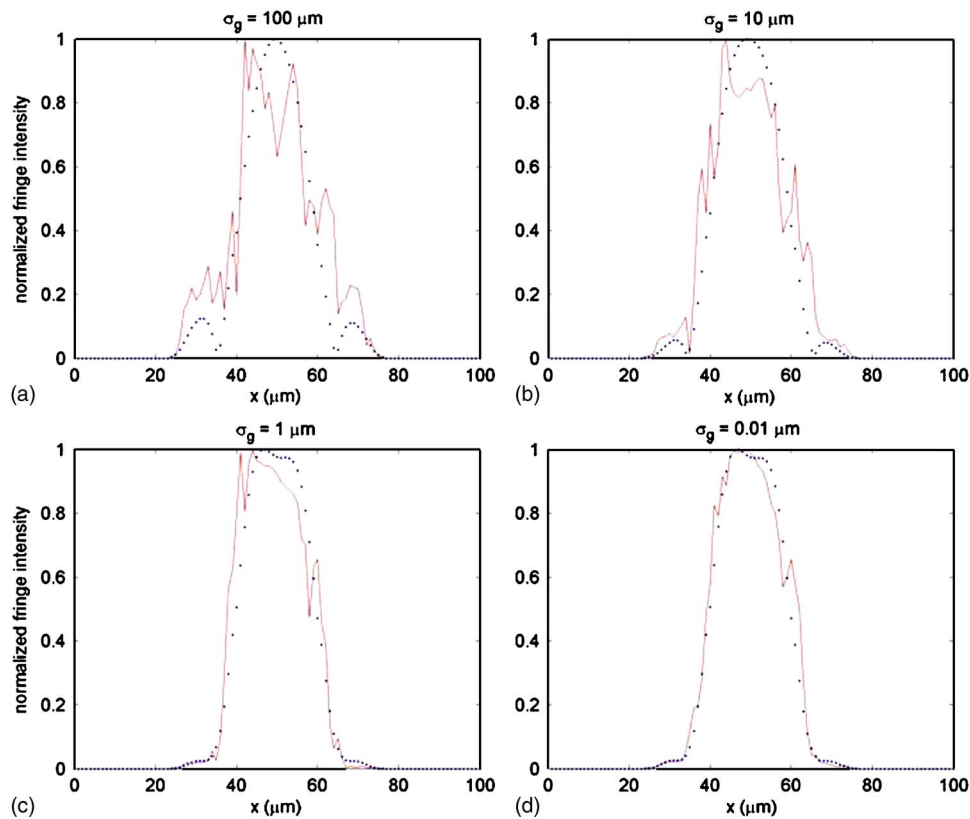
Fig. 5 Simulated normalized fringe intensity for different spatial coherence lengths of Gaussian-Schell model source: σ_g, coherent length of a Gaussian-Schell model source; solid lines, complex fringe signal with speckle; and dotted lines, envelope of complex fringe signal without speckle. Beam spot size at target (σ_s) was set at 100 μm.

first setup (Fig. 3), light is coupled into a multimode fiber to generate many spatial modes. The 100-m-long multimode fiber is mounted on a spool to reduce any variations in mechanical stress that might introduce variable mode coupling. Following the multimode fiber, lens L2 directs light into both sample and reference paths through a broadband beamsplitter (BS). In the second setup using a single-mode fiber, the multimode fiber is removed from the source path of the interferometer. Reflected light from both sample and reference paths are imaged onto a CCD camera (FASTCAM Super 10 K) using a focusing lens (L3). A voice coil with a retroreflector is used in the reference path to provide variable delay (τ) between sample and reference paths. The voice coil is driven by a function generator creating a sinusoidal wave at 0.1 Hz and 10 V_{p-p}. Scan range is 1.6 mm, yielding a fringe carrier fre-

quency f_c=752 Hz. Frame rate of the CCD camera is set at 3000 frames/s sampling the fringe at four points per cycle or twice the Nyquist limit. Integration time of the camera is 50 μs. Output images from the CCD camera are recorded in the digital video (DV) format to avoid any loss in spatial resolution. Incoherent demodulation is used to determine the envelope of the complex fringe signal [Eq. (15)] from recorded 3-D data cubes. Fringe amplitude is determined at each pixel in time (Fig. 4). Other than incoherent demodulation no additional image enhancement is used.

A mill-finished aluminum plate is used as a scattering surface. The rough surface of the aluminum plate produces speckles caused by distorted wavefronts in reflected light. The aluminum plate was tilted slightly to produce a uniform phase gradient and produce linear fringes in the CCD. For comparison, the same physical location covering a 2-mm beam diameter on the aluminum plate is imaged with both single and multimode fiber systems. To maximize fringe visibility and to avoid saturation of CCD photocells, light intensity incident on the CCD camera was adjusted by using a neutral density filter in the detection path of the interferometer.

3 Results

Effect of speckle reduction in OCT imaging was simulated using a Gaussian-Schell model source and Eq. (14) for $I_f(x,\tau)$. For this simulation, the illuminating beam spot [σ_s] was fixed at 100 μm. Simulation results shown in Fig. 5 and
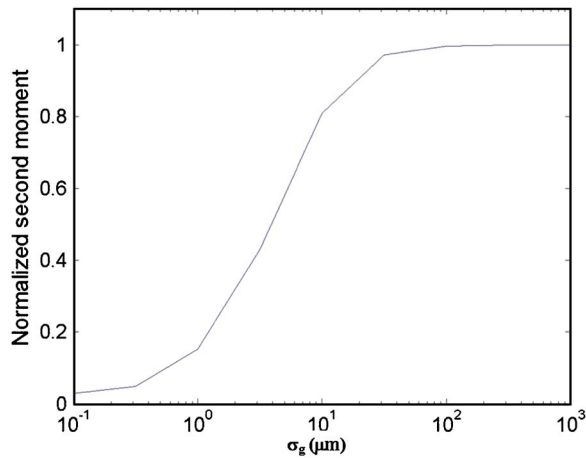
Table 1 Speckle rms variation according to spatial coherence length (σ_g).

σ_g (μm)	Speckle rms
100	0.188
10	0.174
1	0.081
0.1	0.031

Fig. 6 Second moment of normalized complex fringe signal versus spatial coherence length (σ_g).

Fig. 7 CCD camera images of an aluminum plate through (a) single-mode and (b) multimode source fiber. Reference path of interferometer is blocked.

Table 1 are determined for a depth-resolving OCT system with several different spatial coherent lengths (σ_g) corresponding to a Gaussian-Schell model source. In Fig. 5, the dotted lines represent the envelope of the complex fringe signal without speckle, while solid lines are with speckle. The speckle-free case was simulated by removing the random phase term in Eq. (15). Coherent illumination ($\sigma_g = \sigma_s = 100 \ \mu$m) produces the greatest speckle [Fig. 5(a)]. For incoherent illumination, spatial coherence length was set much smaller ($\sigma_g = 0.01 \ \mu$m) than diameter (σ_s) of the illuminating beam [Fig. 5(d)]. Two additional spatial coherence lengths ($\sigma_g = 10, 1 \ \mu$m) in Figs. 5(b) and 5(c), respectively, were investigated to demonstrate speckle reduction with decreasing coherence length. To assess speckle reduction quantitatively, speckle root-mean-square (rms) values were calculated by subtracting computed complex fringe signal with speckle from the speckle-free case. Speckle rms variation with spatial coherence length (σ_g) is shown in Table 1. Entries in Table 1 were computed by averaging 30 simulations for each spatial coherence length (σ_g). Note the logarithmic scale to display σ_g.

To observe difference in sample illumination through single or multimode fibers, light from the reference path was blocked and the aluminum plate was placed in the sample path. Figures 7(a) and 7(b) show intensity images of the sample when illuminated by single-mode and multimode fibers, respectively. Due to a small mode field diameter (5 μm) at the single-mode fiber tip, Airy rings in the illuminated area are observed in Fig. 7(a), whereas relatively flat illumination is evident in the multimode case [Fig. 7(b)].

After restoring the reference path, an interference pattern was measured by the CCD camera corresponding to a 1.6-mm pathlength delay between sample and reference paths. During measurement of the interference pattern, no significant motion artifacts in the fringes, caused by environmental changes, were observed. Measured interference patterns were demodulated using an incoherent demodulation algorithm ( ).

Figures 8(a) and 8(b) show OCT cross-sectional images of the sample at a fixed height, with the normalized complex fringe signal represented along the vertical axis, recorded with
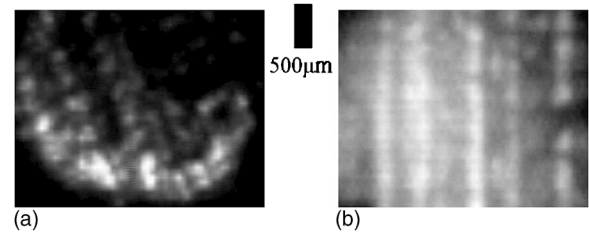
single-mode and multimode fiber systems, respectively. When using the multimode fiber for illumination, speckle is significantly reduced [Fig. 8(b)] compared to that recorded using the single-mode fiber [Fig. 8(a)].

Demodulated interference patterns at a fixed depth recorded with single- and multi-mode fiber systems are shown in (a) and (b) respectively. For comparison, both images were recorded at the same position on the aluminum plate, so surface micro-irregularities of the surface are identical. The image in (a) was recorded after rotating the aluminum plate 20 degrees counterclockwise. The image recorded using the multimode fiber, (b), shows continuous linear fringes corresponding to tilt of the aluminum plate, whereas the image recorded using single mode fiber for illumination, (a), displays disrupted and fragmented bright grey bands over the surface due to speckle.

4 Discussion

Light emitted from a Gaussian-Schell model source considered here has a variable degree of spatial coherence from incoherent to fully coherent. When partially spatial coherent light is launched into the interferometer, the beam may be regarded as an assembly of mutually uncorrelated finite-sized phase cells. In OCT, light input into the interferometer is divided into two beams, which illuminate the sample and the reference mirror. While mirror reflectivity in the reference path is considered constant, the sample has a complex reflectivity function and backscatters incident light. When light reflected from sample and reference paths recombine at the detection plane, cells of the beams overlap and partially interfere. Interference can occur only for light originating from the same phase cell in sample and reference paths. The speckled appearance of the images in is the effect of interference between light backscattered from different particles within a coherence area. With a decrease in the coherence area, speckle reduction is expected, as indicated in Table 1, but as Fig. 5(d) illustrates speckle still exists despite a very small spatial coherence length ($\sigma_g = 0.01 \ \mu$m) corresponding to incoherent illumination.

An interesting point when looking at the complex fringe signal [Eq. (14)] as a random phasor sum is that speckle increases with the second moment of the complex fringe signal, which follows the second moment ($\overline{\alpha^2}$) of amplitude (α_k), not the random phase distribution (ϕ_k). The result of spatial coherence length dependence on the second moment of the complex fringe signal is shown at Fig. 6. The second moment $\overline{\alpha^2}$ of the intensity fluctuation increases as the degree of coher-
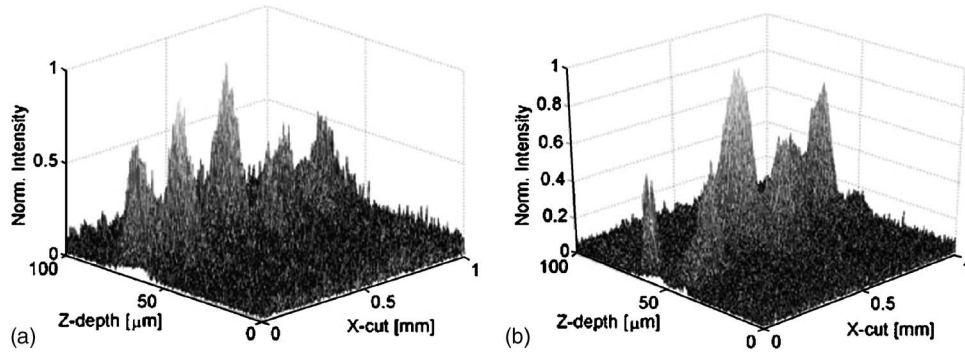
Fig. 8 Cross-section Parallel OCT image recoded from a scattering surface using (a) single-mode and (b) multimode source fiber. Fringe intensities are normalized and correspond to a single depth scan.

ence increases and approaches unity for a spatially coherent beam. The second moment never reaches zero even at the smallest spatial coherence length.

Producing incoherent sources has an inherent trade-off in view of radiation efficiency and the degeneracy parameter.[25] The radiant emittance of a partially spatial coherent source is expressed[30] by

$$E_\nu(\rho) = C_g(\nu)S(\rho,\nu),$$

where the radiation efficiency (C_g) is a proportionality factor between radiant emittance $[E_\nu(\rho)]$ and spectral density $[S(\rho,\nu)]$, and ρ is a position vector of a radiation source point. The radiation efficiency increases monotonically with σ_g, from zero for a completely incoherent source to unity for a completely coherent source.[30] The degeneracy parameter indicates average number of identical photons (same polarization sate) that are contained in a coherence volume. For example, use of spatially incoherent illumination with a thermal light source suffers from a low degeneracy number.[23] The advantage of using a multimode fiber to produce partially spatially coherent light is high number of photons per coherence volume. The source and multimode fiber used in experiments reported here provided 0.3×10^9 photons per coherence volume substantially higher than that provided by a thermal source. Spatial coherence length at the tip of the multimode fiber was calculated[33,34] to be 22 μm by

$$\sigma_g = \left\{ \frac{4\sigma_0^2}{(\pi D NA/2\lambda)^2 - 1} \right\}^{1/2},$$

where D is a core diameter of multimode fiber.

Another advantage of this method to modify coherence properties of the light source is relative simplicity over other methods including use of a ground glass plate or liquid crystals.[30]

In Eq. (1) we assumed amplitude of light returning from the sample is the product of the incident amplitude $[A_i(\xi,\nu)]$ and the local reflectivity $[r(\xi)]$, which is reasonable for the scattering object studied. In tissue, however, the amplitude of light returning from the sample will be a complex function of $A_i(\xi,\nu)$ due to multiple photon paths in the tissue and spatial variation of the refractive index of the tissue.

Speckle reduction using partially spatial coherent sources can be also understood as an incoherent mode summation.

When broadband light is coupled into a multimode fiber, a number of orthogonal spatial modes are generated which are spatially and temporally coherent. Each spatial mode propagates through the multimode fiber at a distinct group velocity producing modal dispersion. After propagating a sufficient length along the fiber, spatial modes become temporally decorrelated due to differences in group velocity. Detected interference is an incoherent sum of interferograms formed between spatial modes. Because each mode forms a statistically independent speckle field, mode summation has the effect of reducing speckle by averaging. The appearance of unbroken grooves in the multimode fiber case [Fig. 9(b)] is consistent with the speckle reduction effect resulting from superposition of many interferograms each representing mutually incoherent spatial modes.

As sample-reference path length delay increases, the delay may compensate the mode separation introduced by the multimode fiber, and the decorrelated modes become correlated again. To avoid this intermodal interference, the multimode fiber should be sufficiently long so that the modal separation is much greater than maximum sample-reference delay time in scanning.

To verify no intermodal interference was present in our system, signal to noise ratios for single mode and multimode cases were measured and compared across the full scanning range (1.6 mm) of the voice coil stage. A mirror was placed in the sample path with a photoreceiver and a 100-μm pinhole in the detection path replaced the CCD camera. We express noise sources in terms of the photocurrent variance σ_i^2. Primary noise sources include receiver (σ_{re}^2), and shot noise (σ_{sh}^2). Intensity noise was omitted because of the small contribution from a mode locked laser.[35] Receiver noise was cal-
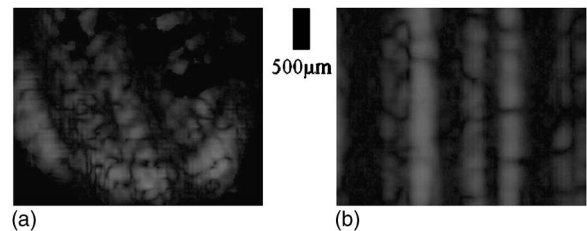

Fig. 9 Low-coherence interferograms recorded from a scattering surface using (a) single-mode and (b) multimode source fibers.

Table 2 Noise comparison between multimode and single-mode source fiber setups.

	σ_{re}	σ_{sh} (multimode)	σ_{sh} (singlemode)
Calculated noise	9.25 μV	10.12 nV	27.2 nV
Measured noise	9.8 μV	11.73 nV	28 nV

culated from the manufacturer's specification. Shot noise is given by,

$$\sigma_{sh}^2 = 2qI_{dc}B,$$

where I_{dc} represents the mean detector photocurrent, and B is the electronic detection bandwidth, and q is the charge on an electron.

Total photocurrent variance is given by

$$\sigma_i^2 = \sigma_{re}^2 + \sigma_{sh}^2.$$

Measured and calculated shot noises are compared in Table 2. The shot noise is calculated from the mean detector photocurrent I_{dc}. Measured shot noise is comparable with calculated values.

We define SNR as peak-to-peak current of the coherence function divided by the total photocurrent standard variance (σ_i). SNRs were 80 and 79 dB over 1.6 mm of reference and sample path delays for single-mode and multimode fiber cases, respectively. The Small difference in SNR between coherent and partially spatial coherent cases indicates degradation of SNR due to the multimode source fiber was insignificant and supports the hypothesis that mode separation between adjacent modes is longer than the scanning range (1.6 mm) after 100 m of travel through the multimode fiber. Mode cross-coupling in the fiber was below the measurement limit over the entire scan (1.6 mm).

5 Conclusion

We proposed and demonstrated a speckle reduction method using a partially spatial coherent source in a Michelson interferometer in a parallel detecting OCT system. Speckle in interferograms recorded using a partially spatial coherent source is substantially reduced compared to the fully coherent case. No degradation in SNR is observed, and no measurable mode cross-coupling is observed in the multimode fiber. A partially spatial coherent source is also preferable for *en face* imaging not only for reducing speckle but also for eliminating Airy rings in the image caused by the small field diameter of most single-mode fibers. Our simulations model a partially spatially coherent source with a Gaussian-Schell model source to indicate speckle reduction in OCT interferograms. As the physical viewpoint, our experiments explain that superposition of coherent modes has the effect of reducing speckle by averaging because each mode forms a statistically independent speckle field. The results of both simulations and experiments indicate that broadband light sources with reduced spatial coherence that provide a large number of photons per coherence volume may be effectively utilized to reduce speckle in OCT interferograms.

References

1. D. Huang, E. A. Swanson, C. P. Lin, J. S. Schuman, W. G. Stinson, W. Chang, M. R. Hee, T. Flotte, K. Gregory, C. A. Puliafito, and J. G. Fujimoto, "Optical coherence tomography," *Science* **254**(5035), 1178–1181 (1991).
2. J. G. Fujimoto, "Optical coherence tomography for ultrahigh resolution in vivo imaging," *Nat. Biotechnol.* **21**(11), 1361–1367 (2003).
3. M. E. Brezinski, G. J. Tearney, S. A. Boppart, B. E. Bouma, E. A. Swanson, J. F. Southern, and J. G. Fujimoto, "High speed catheter based OCT imaging of coronary microstructure," *Circulation* **94**(8), 1494–1494 (1996).
4. W. Drexler, U. Morgner, F. X. Kartner, C. Pitris, S. A. Boppart, X. D. Li, E. P. Ippen, and J. G. Fujimoto, "In vivo ultrahigh-resolution optical coherence tomography," *Opt. Lett.* **24**(17), 1221–1223 (1999).
5. L. Vabre, A. Dubois, and A. C. Boccara, "Thermal-light full-field optical coherence tomography," *Opt. Lett.* **27**(7), 530–532 (2002).
6. M. Ducros, M. Laubscher, B. Karamata, S. Bourquin, T. Lasser, and R. P. Salathe, "Parallel optical coherence tomography in scattering samples using a two-dimensional smart-pixel detector array," *Opt. Commun.* **202**(1–3), 29–35 (2002).
7. S. Bourquin, P. Seitz, and R. P. Salathe, "Two-dimensional smart detector array for interferometric applications," *Electron. Lett.* **37**(15), 975–976 (2001).
8. S. Bourquin, V. Monterosso, P. Seitz, and R. P. Salathe, "Video-rate optical low-coherence reflectometry based on a linear smart detector array," *Opt. Lett.* **25**(2), 102–104 (2000).
9. Z. P. Chen, T. E. Milner, D. Dave, and J. S. Nelson, "Optical Doppler tomographic imaging of fluid flow velocity in highly scattering media," *Opt. Lett.* **22**(1), 64–66 (1997).
10. D. P. Dave, T. Akkin, and T. E. Milner, "Polarization-maintaining fiber-based optical low-coherence reflectometer for characterization and ranging of birefringence," *Opt. Lett.* **28**(19), 1775–1777 (2003).
11. J. F. de Boer and T. E. Milner, "Review of polarization sensitive optical coherence tomography and Stokes vector determination," *J. Biomed. Opt.* **7**(3), 359–371 (2002).
12. D. T. Miller, J. Qu, R. S. Jonnal, and K. Thorn, "Coherence garing and adaptive optics in the eye," *Proc. SPIE* **4956**, 65–72 (2003).
13. A. I. Kholodnykh, I. Y. Petrova, K. V. Larin, M. Motamedi, and R. O. Esenaliev, "Precision of measurement of tissue optical properties with optical coherence tomography," *Appl. Opt.* **42**(16), 3027–3037 (2003).
14. J. Rogowska and M. E. Brezinski, "Evaluation of the adaptive speckle suppression filter for coronary optical coherence tomography imaging," *IEEE Trans. Med. Imaging* **19**(12), 1261–1266 (2000).
15. J. Rogowska and M. E. Brezinski, "Image processing techniques for noise removal, enhancement and segmentation of cartilage OCT images," *Phys. Med. Biol.* **47**(4), 641–655 (2002).
16. J. M. Schmitt, "Restoration of optical coherence images of living tissue using the CLEAN algorithm," *J. Biomed. Opt.* **3**(1), 66–75 (1998).
17. M. D. Kulkarni, C. W. Thomas, and J. A. Izatt, "Image enhancement in optical coherence tomography using deconvolution," *Electron. Lett.* **33**(16), 1365–1367 (1997).
18. K. M. Yung, S. L. Lee, and J. M. Schmitt, "Phase-domain processing of optical coherence tomography images," *J. Biomed. Opt.* **4**(1), 125–136 (1999).
19. J. M. Schmitt, S. H. Xiang, and K. M. Yung, "Speckle in optical coherence tomography," *J. Biomed. Opt.* **4**(1), 95–105 (1999).
20. N. Iftimia, B. E. Bouma, and G. J. Tearney, "Speckle reduction in optical coherence tomography by path length encoded angular compounding," *J. Biomed. Opt.* **8**(2), 260–263 (2003).
21. J. M. Schmitt, "Array detection for speckle reduction in optical co-

herence microscopy," *Phys. Med. Biol.* **42**(7), 1427–1439 (1997).

22. M. Bashkansky and J. Reintjes, "Statistics and reduction of speckle in optical coherence tomography," *Opt. Lett.* **25**(8), 545–547 (2000).

23. B. Karamata, P. Lambelet, M. Laubscher, R. P. Salathe, and T. Lasser, "Spatially incoherent illumination as a mechanism for cross-talk suppression in wide-field optical coherence tomography," *Opt. Lett.* **29**(7), 736–738 (2004).

24. L. Buttner and J. Czarske, "Multi-mode fibre laser Doppler anemometer (LDA) with high spatial resolution for the investigation of boundary layers," *Exp. Fluids* **36**(1), 214–216 (2004).

25. L. Mandel and E. Wolf, *Optical Coherence and Quantum Optics*, pp. 664–666, Cambridge University Press, Cambridge, UK (1995).

26. H. Ambar, Y. Aoki, N. Takai, and T. Asakura, "Fringe contrast improvement in speckle photography by means of speckle reduction using vibrating optical fiber," *Optik (Jena)* **74**(2), 60–64 (1986).

27. H. Ambar, Y. Aoki, N. Takai, and T. Asakura, "Relationship of speckle size to the effectiveness of speckle reduction in laser microscope images using rotating optical fiber," *Optik (Jena)* **74**(1), 22–26 (1986).

28. N. Takai and T. Asakura, "Statistical properties of laser speckles produced under illumination from a multimode optical fiber," *J. Opt. Soc. Am. A* **2**(8), 1282–1290 (1985).

29. J. W. Goodman, *Introduction to Fourier Optics* (1996).

30. L. Mandel and E. Wolf, *Optical Coherence and Quantum Optics*, pp. 298–300, Cambridge University Press, Cambridge, UK (1995).

31. T. Shirai, A. Dogariu, and E. Wolf, "Mode analysis of spreading of partially coherent beams propagating through atmospheric turbulence," *J. Opt. Soc. Am. A* **20**(6), 1094–1102 (2003).

32. M. Young, *Optics and Lasers Including Fibers and Optical Waveguides*, 5th ed., Springer, New York (2000).

33. M. Santarsiero, F. Gori, R. Borghi, G. Cincotti, and P. Vahimaa, "Spreading properties of beams radiated by partially coherent Schell-model sources," *J. Opt. Soc. Am. A* **16**(1), 106–112 (1999).

34. L. Buettner and J. Czarske, "A multimode-fibre laser-Doppler anemometer for highly spatially resolved velocity measurements using low-coherence light," *Meas. Sci. Technol.* **12**(11), 1891–1903 (2001).

35. P. Dufour, G. Rousseau, and N. McCarthy, "Optical noise reduction in a femtosecond Ti:sapphire laser," *Proc. SPIE* **4833**, 894–899 (2002).